Scanning X-ray microdiffraction with submicrometer white beam for strain/stress and orientation mapping in thin films

N. Tamura,[a]* A. A. MacDowell,[a] R. Spolenak,[b] B. C. Valek,[c] J. C. Bravman,[c] W. L. Brown,[b] R. S. Celestre,[a] H. A Padmore,[a] B. W. Batterman[a,d] and J. R. Patel[a,d]

[a]ALS/LBL, 1 Cyclotron Road, Berkeley, CA 94720, USA, [b]Agere Systems, formerly of Bell Labs, Lucent Technologies, Murray Hill, NJ 07974, USA, [c]Department of Material Science and Engineering, Stanford University, Stanford, CA 94305, USA, and [d]SSRL/SLAC, Stanford University, Stanford, CA 94309, USA. E-mail: ntamura@lbl.gov

Scanning X-ray microdiffraction (μSXRD) combines the use of high-brilliance synchrotron sources with the latest achromatic X-ray focusing optics and fast large-area two-dimensional-detector technology. Using white beams or a combination of white and monochromatic beams, this technique allows for the orientation and strain/stress mapping of polycrystalline thin films with submicrometer spatial resolution. The technique is described in detail as applied to the study of thin aluminium and copper blanket films and lines following electromigration testing and/or thermal cycling experiments. It is shown that there are significant orientation and strain/stress variations between grains and inside individual grains. A polycrystalline film when investigated at the granular (micrometer) level shows a highly mechanically inhomogeneous medium that allows insight into its mesoscopic properties. If the μSXRD data are averaged over a macroscopic range, results show good agreement with direct macroscopic texture and stress measurements.

Keywords: X-ray microdiffraction; thin films; strain/stress.

1. Introduction

X-ray diffraction is a powerful, almost century-old, technique that is routinely used in laboratory and synchrotron sources to study the structural properties of materials. Compared with electron probes, X-rays offer the advantages of deeper penetration depth (so that bulk and buried samples can be investigated), virtually no sample preparation and measurement under a variety of different conditions (in air, liquid, gas, vacuum, at different temperatures and pressures).

By combining high-brilliance synchrotron sources, recent progress in X-ray focusing optics, large two-dimensional area fast-detector technology and on-line two-dimensional diffraction-pattern analysis codes, it is now possible to scan samples under a submicrometer polychromatic or monochromatic beam and obtain spatial maps of grain orientation, strain/stress and/or microtopographical information. To obtain these maps, a diffraction pattern is taken and analyzed at each point of the spatial map. EBSD (electron back-scatter diffraction) is the closest equivalent in scanning electron microscopy (SEM) to the technique of scanning X-ray microdiffraction (μSXRD) that is presented in this paper. However, μSXRD is superior to EBSD in strain/stress sensitivity, grain-orientation measurement accuracy and depth-probing capability.

μSXRD using a monochromatic beam and CCD detector has been systematically used for several years at the ESRF (Riekel, 2000). The combination of monochromatic μSXRD with scanning X-ray microfluorescence (μSXRF) has been applied to the microanalysis of fly ash particles (Rindby *et al.*, 1997). Monochromatic μSXRD using an X-ray waveguide capable of a spatial resolution of 100 nm (Müller *et al.*, 2000) has been used for strain mapping of micrometer- and submicrometer-size oxidized lines on silicon (Di Fonzo *et al.*, 2000). The application of monochromatic μSXRD to studies of deformation in bulk polycrystalline materials has been recently demonstrated with a three-dimensional X-ray microscope (Margulies *et al.*, 2001). At the Advanced Light Source, monochromatic μSXRD was used to map the distribution of a given crystalline species in highly inhomogeneous multicompound samples, such as soils. The technique consists of collecting and indexing powder ring patterns at each point. By performing the intensity integration over selected arcs of each of these diffraction patterns, a distribution map of a given mineral species is obtained. This has been applied to earth and environmental science problems and it was recently shown that the synergistic use of three synchrotron-microprobe techniques [μSXRF, microextended X-ray absorption spectroscopy (μEXAFS) and μSXRD (Manceau *et al.*, 2002)] is the right tool to decipher metal sequestration in soil nodules, with the cleaning of contaminated sites as a practical application.

The systematic use of white-beam μSXRD or its combination with monochromatic μSXRD is comparatively far less advanced, and the development of this technique at the Advanced Light Source is the focus of the present paper. The concept of using a white-beam diffraction pattern for texture and strain/stress measurements in polycrystalline thin films has been previously demonstrated at the Advanced Photon Source (Chung *et al.*, 1999; Tamura *et al.*, 1999) and the Advanced Light Source (Chang *et al.*, 1998).

A number of focusing optics have been developed for X-rays during the past decade, including Fresnel zone plates (Lai *et al.*, 1992), refractive compounds lenses (Snigirev *et al.*, 1996), capillaries (Engström *et al.*, 1991; Thiel *et al.*, 1992; Bilderback *et al.*, 1994), waveguides (Spiller & Segmüller, 1974; Jark *et al.*, 1996; Di Fonzo *et al.*, 2000) and Bragg–Fresnel optics (Aristov *et al.*, 1986; Kuznetsov *et al.*, 1994). However, ultra-smooth mirrors in a Kirkpatrick–Baez (KB) orthogonal configuration (Kirkpatrick & Baez, 1948) are the only optics to combine achromaticity, high efficiency and good focus. Since the use of a white beam is an important part of the μSXRD technique described below, achromatic KB mirrors have been chosen as our focusing optics. To obtain a submicrometer-focused beam size with KB mirrors requires the mirrors to have an elliptical shape with submicroradian slope-error tolerance. There are currently two techniques that can do this: the bending of a flat mirror (Iida & Hirano, 1996; MacDowell *et al.*, 2001; Hignette, Rostaing *et al.*, 2001), and the differential coating of a spherical mirror (Ice, Chung, Tischler *et al.*, 2000). Mirror figure errors can be further corrected by ion-beam figuring, as recently demonstrated by Hignette, Peffen *et al.* (2001). All techniques have achieved a spot size of under 0.5 μm. We use the flat-mirror bending technique to achieve a submicrometer focus (MacDowell *et al.*, 2001).

Modern CCD detectors provide a large active area (enabling the collection of a large solid angle of the reciprocal space), fast collection and readout time, adequate dynamic range, and good flood and spatial distortion corrections. CCD detectors are therefore well suited to the fast collection and recording of diffraction patterns, which can be directly fed into an on-line pattern-analysis program.

Sample rotation must, in general, be avoided in μSXRD techniques, not only for data-collection time-efficiency reasons but also because any sample tilt would change the scattering volume even if the sphere of confusion of the goniometer is negligible (Ice, Chung, Lowe *et al.*, 2000). The use of white light instead of monochromatic light is an efficient way to collect in a single shot the large number of

reflections necessary to derive information such as grain orientation and strain. White-beam diffraction data is not sufficient to derive all the strain information in the sample, and the use of a monochromatic beam can be necessary. Therefore the beamline instrumentation is required to be able to easily switch between white and monochromatic beams while illuminating the same area on the sample, independent of the energy. A specific type of monochromator was therefore designed to achieve this goal. An alternative monochromator design for this kind of application has been developed at the Advanced Photon Source (Ice, Chung, Lowe *et al.*, 2000).

The rest of the present paper is divided into four sections. §2 describes the hardware at the microdiffraction end station on beamline 7.3.3 at the Advanced Light Source. §3 explains the algorithm used to analyze the data. §4 shows how the technique can be applied to tackle real materials science problems. Other considerations of the μSXRD technique are addressed in §5.

2. End-station layout and hardware description

A schematic layout of the X-ray microdiffraction beamline and end station is shown in Fig. 1. The X-ray beam from a bending-magnet source (1.9 GeV, 400 mA, 250 μm FWHM × 40 μm FWHM, up to 3 × 0.2 mrad divergence horizontally and vertically, respectively) is 1:1 refocused at the entrance of the hutch by a 700 mm-long platinum-coated silicon toroidal mirror operating at a grazing angle of 5.4 mrad. Water-cooled tungsten slits at the entrance of the hutch act as an adjustable size source for the KB demagnifying optics inside the hutch. This optical arrangement allows a trade off between flux and spot size.

The focusing optics consist of an orthogonal pair of 100 mm-long platinum-coated fused-silica KB mirrors bent to an elliptical shape by applying asymmetric couples through weak-leaf springs. The principle of these KB mirrors has been described elsewhere (MacDowell *et al.*, 2001). The current KB mirrors achieve a spot size of 0.8 × 0.8 μm FWHM, and the setting has proved to be very stable over time when the temperature variations are constrained to be less than 0.2 K. The distance from the center of the last KB mirror to the sample is 120 mm, which gives a sample clearance of 50 mm. The maximum convergence angle onto the sample is 3.7 and 1.6 mrad, respectively, for the vertical and the horizontal focusing mirrors. The KB optics have a limited acceptable aperture of only 130 μrad horizontally and vertically. Flux rates are in the range 10^6–10^7 photon s^{-1} μm^{-2} at ∼10 keV.

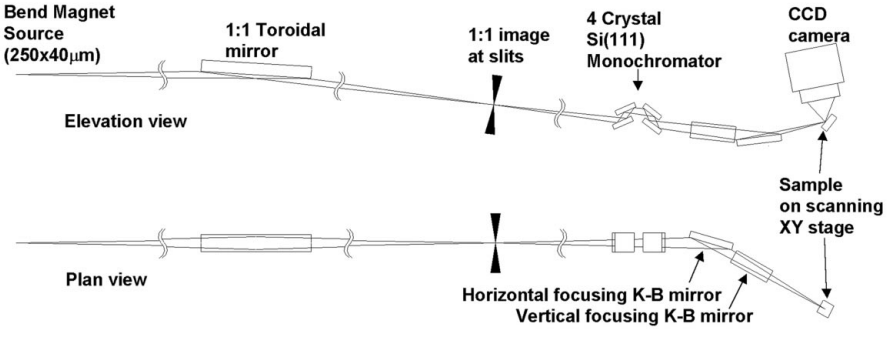

Figure 1
Schematic layout of the beamline and experimental region showing the diffracted X-rays collected by the CCD camera in the 45° reflective geometry. Source to 1:1 toroidal mirror distance is 16 m. Intermediate focus slits to KB mirror distance is 3.4 m. The focused X-ray spot size on the sample is 0.8 × 0.8 μm.

The Si(111) monochromator consists of two identical channel cuts in a +−−+ configuration (Beaumont & Hart, 1974). This arrangement has the property of directing the monochromatic X-rays along the same axis as the incoming white light. The two channel-cut crystals are mounted such that the rotation axis passes through the surface of diffracting surfaces 2 and 3. The energy range available with this monochromator and beamline is between 5.5 and 14 keV as limited by air absorption and the high-energy cut-off of the toroidal mirror (∼50% reflectivity at 14 keV). The off-axis rotation of the crystals allows for them to be rotated out of the way so that white radiation can continue to the KB focusing mirrors. The four-crystal monochromator consists of two rotational stages onto which the two channel-cut crystals are mounted. For Bragg-angle changes the two stages rotate in opposite directions by means of a tape drive, which is driven by a linear slide. We find that the instrument is able to scan in energy and remain on the rocking curve over the available photon energy range without the additional requirement of feedback. The monochromator and KB mirrors are placed inside a compact Plexiglas box filled with a helium atmosphere to improve thermal stability and reduce X-ray air scattering and absorption.

The sample sits on a fine *XY* piezoelectric stage (range of ±50 μm), which is mounted on a coarse *XYZ* Huber stage (range of ±5 mm in *XY* and ±10 mm in *Z*). The sample can also be mounted on a heating stage for experiments requiring high temperatures (up to 873 K). The diffraction patterns are collected with a SMART 6000 Bruker CCD (active area of 90 × 90 mm). The sample is usually mounted in a 45° reflective geometry (see Fig. 1) with the CCD on a vertical slide at a distance of approximately 35 mm from the sample area illuminated by the beam. This allows for the collection of a large solid angle of the reciprocal space without having to move the detector. When illuminated with the white beam (energy range of 5.5–14 keV), a (111)-oriented Al grain will give ∼15 reflections. Samples with larger lattice constants and lower symmetries give even more reflections (more than 100 for YBCO and sapphire, for instance).

3. Software

Laue (white-beam) patterns are extensively used to determine single-crystal orientation with laboratory sources. At synchrotron sources, Laue diffraction has been used to analyze rapid reactions in complex molecules, such as enzymes and proteins (so-called time-resolved Laue diffraction) (Moffat, 1997; *International Tables for X-ray Crystallography*, 2000, Vol. F), but its use in the materials science community has so far been limited. Laue patterns obtained at synchrotron sources using submicrometer focused X-ray beams yield quantitative high-accuracy information on both orientation and strain within the illuminated volume. The potential to obtain accurate strain information from the Laue patterns obtained was first addressed by a group at the Oak Ridge National Laboratory (Chung & Ice, 1999; Chung *et al.*, 1999; Tamura *et al.*, 1999). However, in order to obtain orientation and strain maps, the μSXRD technique requires a fast on-line and totally automated code, which directly and iteratively downloads a series of collected CCD images, finds the reflection positions, indexes them, and calculates the orientation matrix and strain/stress tensor. We have developed such a software package called

X-MAS (X-ray microdiffraction analysis software), and it is under continuous development at the ALS. The detailed operation of this complex code will be described below. It is based on a previous algorithm described by Chung & Ice (1999).

The CCD diffraction image first receives image-intensity and spatial-distortion corrections (dark-current removal, flood-field correction, spatial correction). Peak positions are then automatically found using a peak-searching routine. Two-dimensional local maxima peak search routines have proved to be more efficient than convolution-based routines, especially in the case of complex-shaped peaks from plastically deformed samples. These peaks are classified according to their integrated intensity and are then fit to a two-dimensional Gaussian, Lorentzian or Pearson VII function, which allows the instrument to achieve subpixel resolution on the position of the peaks on the CCD. This resolution is possible because the divergence of the beam and the tails of its Lorentzian profile allow several pixels to be illuminated for each reflection. The best fit is usually obtained with a two-dimensional Lorentzian function. The accuracy to which the peak positions are fit is one of the limiting factors for strain accuracy.

Once the peak positions are found, the pattern can be indexed with *hkl* Miller indices. For the indexing of the Laue pattern, a subset N of the most intense reflections is first considered in the reflection list. Using the instrument geometry calibration procedure described below, the direction of the incident beam $\mathbf{k}_{\rm in}$ and the position of the illuminated area in the sample are known relative to the CCD camera position. The peak positions on the CCD allow the calculation of the outgoing reflected-beam directions $\mathbf{k}_{\rm out}$. Assuming elastic scattering (*i.e.* $|\mathbf{k}_{\rm in}| = |\mathbf{k}_{\rm out}|$), the direction of the experimental scattering vector is

$$\mathbf{q}_{\rm exp} = \mathbf{k}_{\rm out} - \mathbf{k}_{\rm in}. \tag{1}$$

The angles between these $\mathbf{q}_{\rm exp}$ vectors are tabulated into an 'experimental' list [$N(N-1)/2$ items] and then compared with a 'reference' list of angles between theoretical scattering vectors $\mathbf{q}_{\rm ref}$ computed from the crystalline structure of interest and the energy bandpass of the polychromatic beam. The code looks for angular matches between triplets of reflections within an adjustable angular tolerance. Each triplet and their corresponding (*hkl*) indices are then used to calculate a trial orientation matrix and a complete list of reflections that should be visible on the CCD for the considered energy bandpass, CCD dimensions and geometry. The best match is the triplet that is able to index the largest number of experimental reflections. Many considerations, such as crystal symmetry, structure factor and number N of selected experimental intense reflections, are used to limit the number of possibilities. For instance, for a Laue pattern taken on a single-crystal region, a small value of N is used (we know that all the most intense reflections are coming from the same grain), whereas in the case of a pattern taken in a polycrystalline region this N value should be increased to allow the algorithm to index a set of overlapping diffraction patterns coming from different illuminated grains. The main advantage of this algorithm is the possibility of automatically separating the contribution of different grains in a single pattern and of indexing overlapping diffraction patterns from randomly oriented grains. The use of triplets instead of pairs of reflections like in Chung & Ice (1999) renders the algorithm more robust. The algorithm is able to differentiate and index more than ten overlapping grains.

Knowing the positions of the reflections on the CCD, it is easy to calculate their Bragg angle θ if the exact position of the CCD with respect to the incoming beam and the point of 'impact' on the sample are known (geometrical parameters). The number of independent parameters is five: the X and Y coordinates of the 'center channel' on the detector, the distance from this center channel to the 'point of impact' on the sample, and two angular parameters describing the tilts of the detector with respect to the incoming beam direction. Two methods can be used to refine the geometrical parameters. The first is a triangulation technique whereby several images are collected at different CCD distances from the sample and ray-traced back to the origin of the reflective beams. Moving the CCD, however, introduces a sixth parameter (translation angular direction of the CCD), which adds additional complications and errors. The second method uses a non-linear least-squares refinement of a Laue pattern from a 'calibration' sample. With this method all five parameters are obtained and no CCD movement is required. An unstrained single crystal with no defects (short extinction length) and with sufficiently large lattice constants to give enough reflections in the Laue pattern produces a good calibration. A (001)-oriented perfect silicon crystal would give 40–60 sharp reflections on the CCD. The ideal case is when the calibration crystal is directly part of the sample. For instance, in the case of thin films deposited on a silicon substrate, the reflections from the relatively unstrained wafer underneath can be used for measuring the geometrical parameters. Refinements of these parameters are obtained by minimizing the function

$$\alpha_0 = \sum_i w_i(\alpha_i^{\rm th} - \alpha_i^{\rm exp})^2 / \sum_i w_i, \tag{2}$$

where $\alpha_i^{\rm th}$ and $\alpha_i^{\rm exp}$ are the theoretical and experimental values of the differences in angle between two scattering vectors $\mathbf{q}_{\rm exp}$, and w_i are weighting factors. This of course presupposes that the Laue pattern of the reference sample is properly indexed. The sum is over all pairs of reflections visible on the CCD.

The minimization procedure used for calibration can also be used for refinement of the deviatoric strain tensor (unit-cell distortion). Here we now have the geometrical parameters fixed while the lattice parameters a, b, c, α, β, γ are floating. The distorted unit-cell parameters can then be obtained. White-beam patterns only allow the measurement of unit-cell distortions, not changes in the unit-cell volume (the dilatational or hydrostatic strain), so that only relative values of a, b and c can be refined. The transformation matrix $\mathbf{t}_{ij}$, which defines the transformation from the unstrained crystal vectors to the distorted unit-cell vectors, can then be derived. The $\mathbf{t}_{ij}$ tensor contains both distortional components and rigid-body rotation terms. The rotational component is antisymmetric and can be eliminated by

$$\varepsilon'_{ij} = (t_{ij} + t_{ji})/2 - I_{ij}, \tag{3}$$

where I_{ij} is the identity matrix.

ε'_{ij} is, by definition, the deviatoric strain tensor within the X-ray illuminated volume. The complete strain tensor is the sum of the deviatoric tensor ε'_{ij} and of the dilatational tensor Δ,

$$\varepsilon_{ij} = \varepsilon'_{ij} + \Delta, \tag{4}$$

with $\Delta = \delta I_{ij}$, where $\delta = (\varepsilon_{11} + \varepsilon_{22} + \varepsilon_{33})/3$ is called the dilatational (or hydrostatic) strain.

Since

$$\varepsilon'_{11} + \varepsilon'_{22} + \varepsilon'_{33} = 0, \tag{5}$$

the deviatoric tensor consists of only five independent terms. The dilatational component consists of a remaining single unknown δ. This means that the full six-term strain component can in principle be determined from a single white-beam diffraction image plus a knowledge of the absolute lattice value of a single reflection. The stress tensor is derived from the strain tensor and literature values of the anisotropic stiffness constants C_{ijkl} as

$$\sigma_{ij} = C_{ijkl}\,\varepsilon_{kl}. \quad (6)$$

In many cases, the measurement of the dilatational component is not necessary since the deviatoric part contains all the shear information relevant for the study of deformation. In the case of thin films, the dilatational component can be estimated by defining a limiting condition on the out-of-plane stress. It can be assumed that $\sigma_{zz} = 0$ for a blanket thin film as it is unconstrained in the out-of-plane z direction. In cases where a knowledge of the dilatational component is necessary (for instance, in triaxially constrained materials), it can be obtained by measuring the energy of one reflection. This measurement is performed by scanning the monochromator and recording CCD diffraction images for each energy point. The monochromator energy at which the diffraction spot is the most intense defines the wavelength necessary to determine the lattice spacing (Tamura *et al.*, 1999).

4. Applications

μSXRD can be used to map orientation and strain/stress in thin single-crystal or polycrystalline films with a grain size larger than 1 μm. The spatial resolution is nominally given by the step size used for the scans, which is generally slightly smaller than the actual beam size measured at FWHM. The resolution of the orientation maps can be increased by grain-profile interpolation. Since each grain is illuminated more than once in the scan, a discrete intensity profile of the shape of the grain can be obtained from a selected set of reflections. The boundaries of the intensity profile are not sharp because of the Lorentzian nature of the X-ray beam profile, and a grain is still visible (with a very low intensity) a few micrometers after its boundary has been crossed. By using linear interpolation, a grain profile shape (convoluted with the X-ray beam profile) is obtained. Grain boundaries are then obtained by intersecting the normalized grain profiles of all grains.

The two examples described below are measurements on Al or Cu thin films that were designed to simulate integrated-circuit interconnects and to study failure mechanisms due to the transport of metal atoms along the wire length when a very high current density is applied. This phenomenon is known as electromigration and generates high stress gradients in the wires (Blech & Herring, 1976). The width of modern interconnects are typically in the micrometer and submicrometer range, and grain sizes are of the order of a few micrometers. Their dimensions are well matched to white-beam μSXRD experiments on individual lines. The capabilities of the technique were first used to perform strain and orientation mapping both at room temperature and during a temperature cycle (see §4.1 below). A blanket-film experiment is particularly relevant for evaluating the technique, because data can be averaged over several grains and statistically compared with results obtained with strain/stress macro-measurement techniques, which do not have submicrometer spatial resolution. The technique was then applied to the study of electromigration-related failure, which is a more complex problem that is dependent on the line microstructure (§4.2).

4.1. Thermal stress measurements in Al(Cu) interconnects

The samples consist of patterned Al (with 0.5% wt Cu) lines (length 30 μm, thickness 0.7 μm, width 4.1 and 0.7 μm) sputter deposited on an Si wafer and buried under a glass (SiO_2) passivation layer (0.7 μm thick). As a comparison, data has also been taken on unpassivated Al (0.5% wt Cu) bond pads, which simulate blanket films.

Fig. 2 shows orientation and deviatoric stress maps on a 5 × 5 μm region in the unpassivated pad (Fig. 2*a*) and on the 4.1 μm-wide (Fig. 2*b*) and 0.7 μm-wide (Fig. 2*c*) passivated lines. On the microscopic scale, the stress in the pad is far from homogeneous: the stress is triaxial ($\sigma'_{xx} \neq \sigma'_{yy} \neq \sigma'_{zz}$) with local differences reaching 60 MPa. On the macro scale the stress in the pad appears to be on average biaxial and in tension (the average in-plane deviatoric stresses are $\langle\sigma'_{xx}\rangle \simeq \langle\sigma'_{yy}\rangle \simeq 22.7$ MPa), which is consistent with macroscopic stress measurements using wafer curvature and conventional X-ray diffraction techniques. The absolute average biaxial stress can be calculated as (Tamura *et al.*, 2002)

$$\langle\sigma_{\rm b}\rangle = \langle(\sigma'_{xx} + \sigma'_{yy})/2 - \sigma'_{zz}\rangle = -3\langle\sigma'_{zz}\rangle/2 \simeq 68\,{\rm MPa}. \quad (7)$$

The lines displayed local variations of 60–80 MPa in stress for the 4.1 μm line and up to 140 MPa for the 0.7 μm line. As the line gets narrower, the level of stress gets higher and, on average, shifts from biaxial to triaxial. The orientation maps in Fig. 2 show the change in the microstructure from polycrystalline in the pad and in the 4.1 μm line to 'bamboo'-type for the 0.7 μm line.

Fig. 3 shows a temperature-cycle curve obtained between 298 and 628 K by scanning a 9 × 9 μm area of the unpassivated pad at each temperature step. The pad was annealed to 663 K prior to the experiment to eliminate relaxation effects. The curve was obtained by averaging the stress data over the scanned area and calculating the average biaxial stress using (7). The results show good agreement with the average stress–temperature curves obtained with conventional macrotechniques (Venkatraman *et al.*, 1990); however, the μSXRD technique shows, on the local scale, a high degree of spatial complexity that macroscopic techniques are unable to resolve. The insets in Fig. 3 show the spatially resolved local variations of the stress as revealed by μSXRD at different temperatures. Large intergranular and intragranular stress variations have been measured, which indicate that local parameters such as grain orientation, grain initial stress, grain size and type of grain boundaries play a crucial role in explaining the inhomogeneous yielding mechanisms of polycrystalline thin films during thermal cycling.

Temperature-cycling experiments between 298 and 618 K were carried out on similar samples (Valek *et al.*, 2001). One striking feature observed for the unpassivated pad is that some grains already started to yield while still in the tensile region of the average stress–temperature curves, a behavior explained by the large distribution of stresses and yield stresses in the sample before the experiment (Tamura *et al.*, 2002).

This particular example shows the ability of μSXRD to provide quantitative data such as grain orientation, structure and stress at the local level in polycrystalline metallic thin films, thus greatly improving our understanding of and the modeling of material mechanical properties.

4.2. Electromigration in damascene Cu interconnects

The samples consist of pure Cu interconnect lines (length 100 μm, thickness 1 μm, width 1.1 μm) passivated under a boron nitride layer. The interconnects were produced by the damascene technique, where the copper is plated out into open channels and then mechanically polished to the desired thickness. Fig. 4 shows a region of a copper interconnect that has undergone electromigration testing (Meier Chang, 2002). Fig. 4(*a*) shows a high-voltage scanning electron microscope (HVSEM) image taken just after the electromigration test, near the anode end. There is a metal build-up region, indicated in the figure by a black circle, which appears as a slightly darker region in the image. The corresponding orientation and resolved

shear stress maps of the same part of the line obtained by μSXRD are displayed in Figs. 4(*b*) and 4(*c*), respectively. The resolved shear stresses are calculated from the measured deviatoric stresses with consideration of the 12 independent {111}/⟨110⟩ glide systems of Cu. The grain structure in that particular region of the line has a random out-of-plane orientation and a near-bamboo structure. The indices next to the map in Fig. 4(*b*) indicate the approximate out-of-plane orientation of some of the grains. At the location of the local buildup region, the resolved shear stress dramatically increases to reach a maximum value of about 600 MPa. The orientation map shows that metal has accumulated at the interface of a (111) bamboo grain just before the location of a (115) twin and after a series of small randomly oriented grains. Surface diffusion at the interface between Cu and the passivation layer is the dominant diffusion mechanism in Cu interconnects (Hu *et al.*, 1999). Surface diffusivity in Cu is highly anisotropic (Cousty *et al.*, 1981), thus a highly inhomogeneous diffusion path is generated for the atomic flow in Cu lines. In our particular example the small-grain regions and the (111) grains, because of their particular out-of-plane as well as in-plane orientations, are a fast diffusion path compared with the region of the (115) twin, where the surface diffusion channels happen to be almost perpendicular to the direction of the atomic flow. The region with the (115) twin therefore constitutes a bottleneck for atomic diffusion. A detailed μSXRD correlative study of metal accumulation and depletion areas with anisotropy of surface diffusivity in Cu lines was recently addressed (Meir Chang, 2002). The width of the Bragg reflections also contains information on the dislocation density and provides an indication of the level of stress and plastic deformation inside a particular grain (Barabash *et al.*, 2001). The peak width of the (113) reflection is plotted in Fig. 4(*d*) as a function of the position along the 2 μm-long (111) grain that contains the (115) blocking twin. The peak is clearly broader in the build-up region next to the twin boundary, which indicates local plastic deformation.

The above study shows that electromigration-induced failures in interconnect metal lines are highly dependent on the microstructure and initial stress state of the samples. The capability demonstrated by this technique to non-destructively probe local grain structure and stress is particularly relevant to the understanding of microstructure-related failure mechanisms and to the prediction of where the line is likely to fail during service. This technologically important problem is shown to be much more complex when the line dimensions shrink to a size where microstructural local effects can no longer be neglected.

5. Other considerations of the μSXRD techniques

μSXRD using a white microbeam can be used on a variety of different samples, especially thin films. However, the applicability of the white-beam method is limited by the size of the polycrystal grains. In order to obtain a diffraction pattern with well defined reflection spots, the grain size must be larger than or of the order of magnitude of the actual beam size. For samples with very small grains (< 100 nm), the white-beam technique is not applicable and a

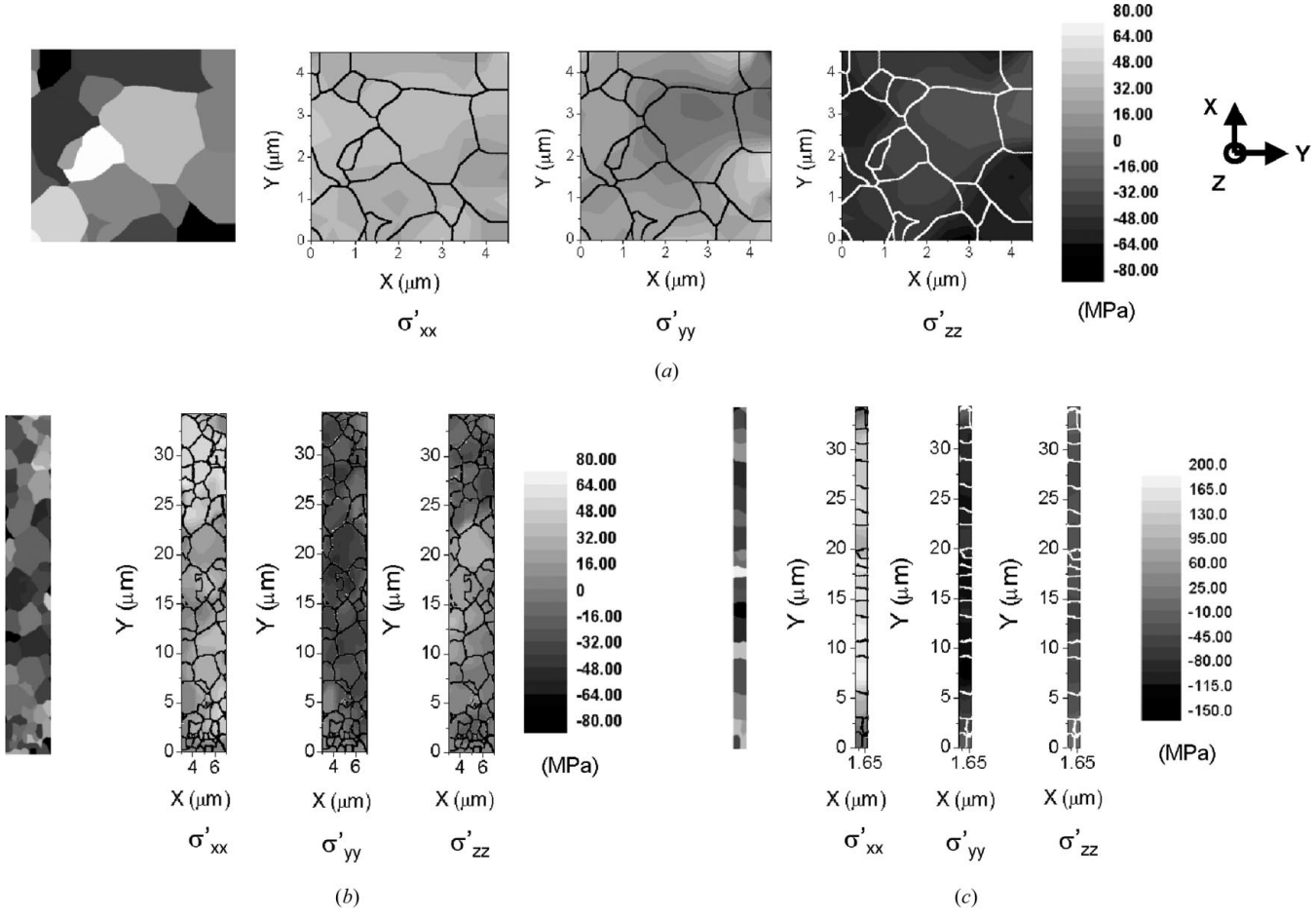

Figure 2
Orientation and deviatoric stress maps for a 0.75 μm-thick Al (0.5% Cu) thin film. Three structures are shown: a 5 × 5 μm area within an unpassivated pad (*a*) and passivated lines of width 4.1 μm (*b*) and 0.7 μm (*c*). The gray-level differences between grains in the orientation map are correlated to their in-plane orientation.

monochromatic beam must be used. The diffraction pattern is then a powder ring pattern, which can also be indexed. Using the $\sin^2\psi$ technique, the biaxial stress of the thin film can be derived from the deviation of the powder ring shape from the unstrained lattice parameters. The analysis of the powder ring pattern can be fully automated in a similar way to the analysis of the white-beam Laue patterns, and strain/stress maps of thin films would be a natural output of monochromatic μSXRD. This technique is currently under development at the ALS (Goudeau *et al.*, 2002).

Concerning the resolution, two factors have to be taken into account: beam size and step size. A smaller white-beam spot size would increase the spatial resolution, and it was recently demonstrated that KBs can achieve 0.2 μm focus FWHM (Hignette, Peffen *et al.*, 2001). However, resolution is, up to a certain point, a function of the step size used for the scans, because the beam profile out of the KBs has typically a Lorenzian shape so that the core of the illuminated area is approximately an order of magnitude smaller than the actual beam size measured at FWHM. Using a 0.25 μm step size for the scans, we were actually able to see differences of orientation and strain with a greater resolution than would be expected from the actual FWHM beam size of 0.8 μm for our beam

Other practical challenges concern the huge amount of generated data. Each CCD image consumes 2 MB of memory in 1024 × 1024 binning mode, which requires us to use either large data-storage capacity or fast data reduction. The other current bottleneck for white-beam μSXRD is the data-collection time, which is currently limited on our station by the readout time of our CCD (several seconds), whereas the exposure time for a 1 μm-thick Cu film only requires 0.1–1 s. A typical scan contains about 1000 data points, which represent a scan time of about 3 h. The replacement of the current system with a subsecond readout-time CCD, smaller pixel size and large active area (at least 100 mm) would shrink these scan times to about 20 min while increasing the strain sensitivity. Higher-powered computers and analysis algorithms with higher efficiency are among other practical considerations that can decrease the data-reduction time to match the collection time. The use of clusters for parallel computing of several diffraction patterns will allow users to have real-time outputs from their scans.

6. Conclusions

We have described the technique of scanning X-ray microdiffraction (μSXRD) and its application to two thin-film materials science problems. The technique has come about as a result of the availability of high-brightness synchrotron sources, fast large-area X-ray CCD detectors and high-speed on-line computing capabilities for data reduction. White-beam μSXRD can provide unique information on the orientation and stress of polycrystalline materials at the scale of their grain size, the so-called mesoscale (typically 0.1–10 μm). The technique is effectively able to probe *in situ* inter- as well as intragranular strain variations in materials experiencing external thermal or mechanical stress. The length scale reached by this technique is small enough to probe local intergranular strain and orientation variations while remaining large enough for statistical representation over a large number of grains, thus allowing macroscopic properties to be linked with microscopic ones. This link is particularly important

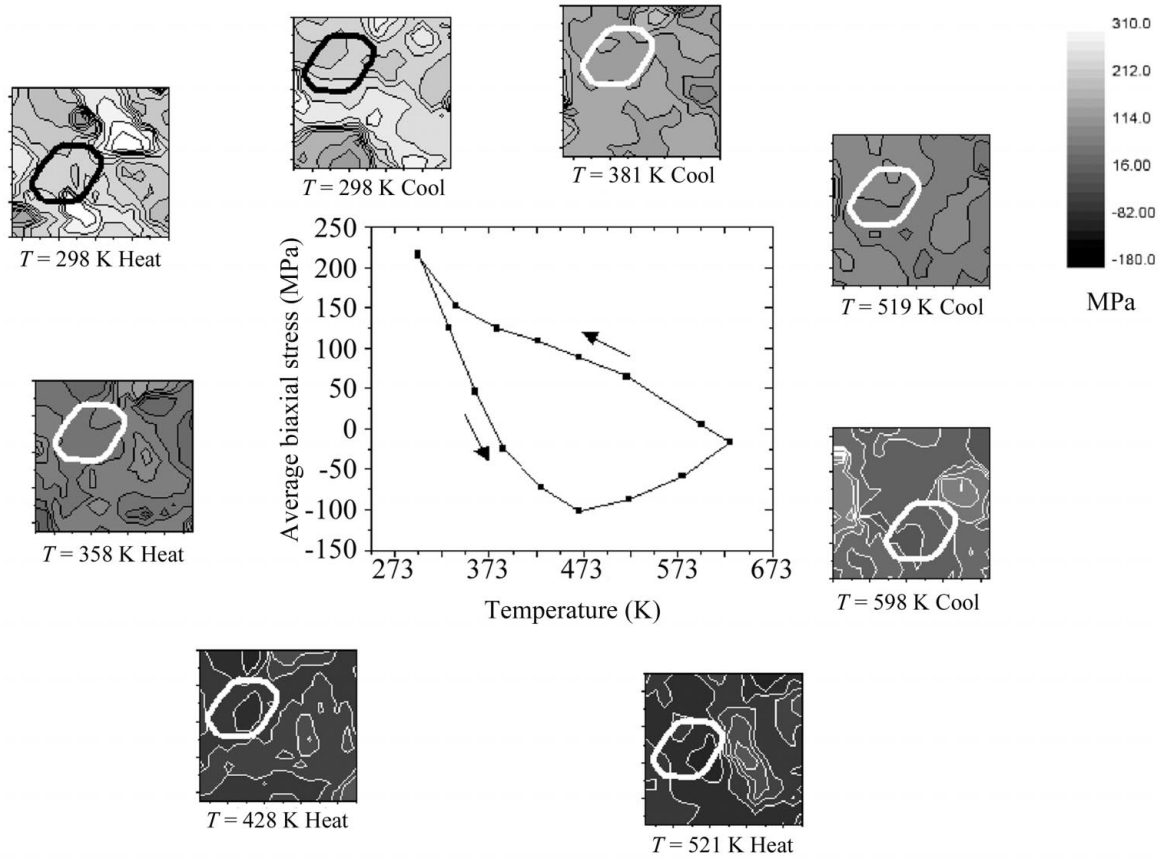

Figure 3
Thermal cycling curve of a 9 × 9 μm area of an Al (0.5% Cu) unpassivated pad. The plot shows the evolution of the average biaxial stress during the process. The inserts show the spatially resolved local stresses on the scanned area at eight different temperatures upon heating and cooling. Because of sample drift, the area of interest had to be repositioned at each temperature and is not exactly identical in each scan. The contour of one particular grain is outlined in each insert.

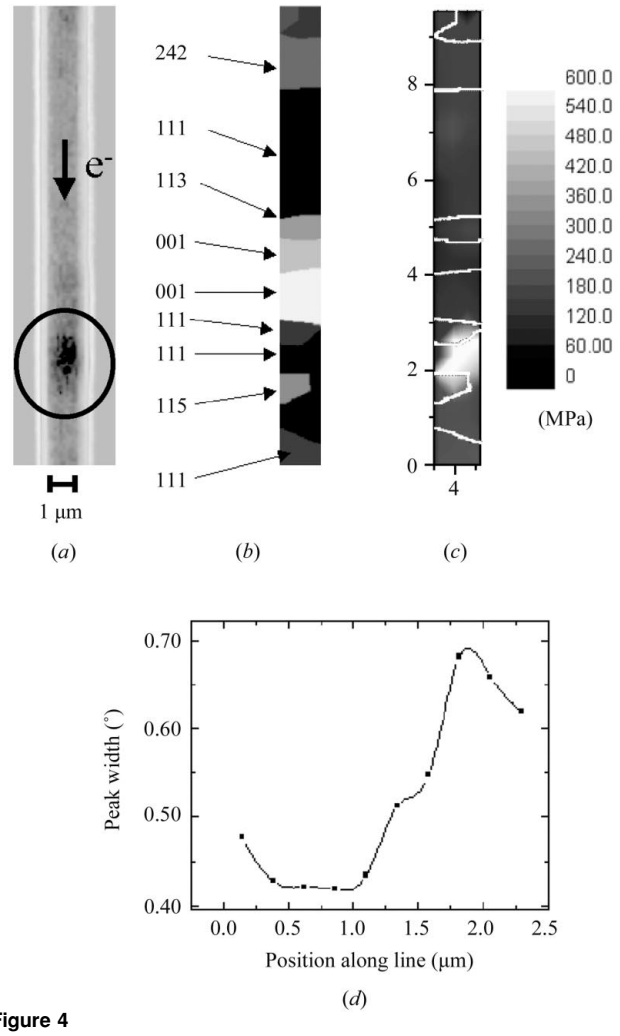

Figure 4
(*a*) Post-electromigration HVSEM image of a portion of a 1.1 μm-wide Cu line. The dark area in the circle indicates a metal accumulation area. (*b*) Corresponding grain map obtained by μSXRD. The indices indicate the approximate out-of-plane orientation of some of the grains. (*c*) Corresponding resolved shear stress map. A high-stress region of 600 MPa is visible in a (111) grain at a boundary of a (115) twin. (*d*) Width of the (113) reflection of the (111) orientated grain containing the (115) twin *versus* position along the grain's 2 μm length.

for high-performance modern materials, whose properties (such as strength) and failure mechanisms are highly dependent on their microstructure. The technique will develop over the coming years, and it is likely to yield important insights into the mesoscale properties of materials. These insights will have far-reaching importance in the understanding of matter, just as the macro X-ray diffraction technique has over the last century. In addition to the X-ray microdiffraction end station at the Advanced Light Source, two beamlines with similar white/monochromatic-beam capabilities exist at the Advanced Photon Source on undulator sources (Ice, Chung, Tischler *et al.*, 2000; Ice, Chung, Lowe *et al.*, 2000), while an X-ray microdiffraction end station using virtually the same optics as the ALS has been implemented at the Pohang Light Source (beamline 1B2).

The Advanced Light Source is supported by the Director, Office of Science, Office of Basic Energy Sciences, Materials Sciences Division, of the US Department of Energy under Contract No. DE-AC03-76SF00098 at Lawrence Berkeley National Laboratory. We thank Intel for the partial funding of the end station and the anonymous reviewers for valuable comments on the paper.

References

Aristov, V. V., Basov, Y. A., Redkin, S. V., Snigirev, A. A. & Yunkin, V. A. (1986). *Nucl. Instrum. Methods Phys. Res. A*, **261**, 72–75.
Barabash, R., Ice, G. E., Larson, B. C., Pharr, G. M., Chung, K.-S. & Yang, W. (2001). *Appl. Phys. Lett.* **79**, 749–751.
Beaumont, J. H. & Hart, M. (1974). *J. Phys. E*, **7**, 823–829.
Bilderback, D. H., Hoffman, S. A. & Thiel, D. J. (1994). *Science*, **263**, 201–203.
Blech, I. A. & Herring, C. (1976). *Appl. Phys. Lett.* **29**, 131–133.
Chang, C.-H., MacDowell, A. A., Thompson, A. C., Padmore, H. A. & Patel, J. R. (1998). *Am. Inst. Phys. Conf. Proc.* **449**, 424–426.
Chung, J.-S. & Ice, G. E. (1999). *J. Appl. Phys.* **86**, 5249–5255.
Chung, J.-S., Tamura, N., Ice, G. E., Larson, B. C., Budai, J. D. & Lowe, W. P. (1999). *Mater. Res. Soc. Proc.* **563**, 169–174.
Cousty, J., Peix, R. & Perraillon, B. (1981). *Surf. Sci.* **107**, 586–604.
Di Fonzo, S., Jark, W., Lagomarsino, S., Giannini, C., De Caro, L., Cedola, A. & Muller, M. (2000). *Nature* (*London*), **403**, 638–640.
Engström, P., Larsson, S., Rindby, A., Buttkewitz, A., Garbe, S., Gaul, G., Knöchel, A. & Lechtenberg, F. (1991). *Nucl. Instrum. Methods Phys. Res. A*, **302**, 547–552.
Goudeau, P., Villain, P., Tamura, N., Celestre, R. S. & Padmore, H. A. (2002). *J. Phys. IV*, **12**, 409–415.
Hignette, O., Peffen, J.-C., Alvaro, V., Chinchio, E. & Freund, A. K. (2001). *Proc. SPIE*, **4501**, 43–53.
Hignette, O., Rostaing, G., Cloetens, P., Rommeveaux, A., Ludwig, W. & Freund, A. (2001). *Proc. SPIE*, **4499**, 105–116.
Hu, C.-K., Rosenberg, R. & Lee, K. Y. (1999). *Appl. Phys. Lett.* **74**, 2945–2947.
Ice, G. E., Chung, J.-S., Lowe, W., Williams, E. & Edelman, J. (2000). *Rev. Sci. Instrum.* **71**, 2001–2006.
Ice, G. E., Chung, J.-S., Tischler, J. Z., Lunt, A. & Assoufid, L. (2000). *Rev. Sci. Instrum.* **71**, 2635–2639.
Iida, A. & Hirano, K. (1996). *Nucl. Instrum. Methods Phys. Res. B*, **114**, 149–153.
Jark, W., Di Fonzo, S., Lagomarsino, S., Cedola, A., Fabrizio, E. D., Bram, A. & Riekel, C. (1996). *J. Appl. Phys.* **80**, 4831–4836.
Kirkpatrick, P. & Baez, A. V. (1948). *J. Opt. Soc. Am.* **38**, 766–774.
Kuznetsov, S. M., Snigireva, I. I., Snigirev, A. A., Engstrom, P. & Riekel, C. (1994). *Appl. Phys. Lett.* **65**, 827–829.
Lai, B., Yun, W. B., Legnini, D., Xiao, Y., Chrzas, J., Viccaro, P. J., White, V., Bajikar, S., Denton, D., Cerrina, F., Di Fabrizio, E., Gentili, M., Grella, L. & Baciocchi, M. (1992). *Appl. Phys. Lett.* **61**, 1877–1879.
MacDowell, A. A., Celestre, R. S., Tamura, N., Spolenak, R., Valek, B., Brown, W. L., Bravman, J. C., Padmore, H. A., Batterman, B. W. & Patel, J. R. (2001). *Nucl. Instrum. Methods Phys. Res. A*, **467/468**, 936–943.
Manceau, A., Tamura, N., Marcus, M. A., MacDowell, A. A., Celestre, R. S., Sublett, R. E., Sposito, G. & Padmore, H. A. (2002). *Am. Mineral.* **87**, 1494–1499.
Margulies, L., Winther, G. & Poulsen, H. F. (2001). *Science*, **291**, 2392–2394.
Meier Chang, N. (2002). PhD thesis, Stanford University, USA.
Moffat, K. (1997). *Methods Enzymol. B*, **277**, 433–447.
Müller, M., Burghammer, M., Flot, D., Riekel, C., Morawe, C., Murphy, B. & Cedola, A. (2000). *J. Appl. Cryst.* **33**, 1231–1240.
Riekel, C. (2000). *Rep. Prog. Phys.* **63**, 233–262.
Rindby, A., Engström, P. & Janssens, K. (1997). *J. Synchrotron Rad.* **4**, 228–235.
Snigirev, A., Kohn, V., Snigireva, I. & Lengeler, B. (1996). *Nature* (*London*), **384**, 49–51.
Spiller, E. & Segmüller, A. (1974). *Appl. Phys. Lett.* **24**, 60–61.
Tamura, N., Chung, J.-S., Ice, G. E., Larson, B. C., Budai, J. D., Tischler, J. Z., Yoon, M., Williams, E. L. & Lowe, W. P. (1999). *Mater. Res. Soc. Proc.* **563**, 175–180.
Tamura, N., MacDowell, A. A., Celestre, R. S., Padmore, H. A., Valek, B., Bravman, J. C, Spolenak, R., Brown, W. L., Marieb, T., Fujimoto, H., Batterman, B. W. & Patel, J. R. (2002). *Appl. Phys. Lett.* **80**, 3724–3727.
Thiel, D. J., Bilderback, D. H., Lewis, A. & Stern, E. A. (1992). *Nucl. Instrum. Methods Phys. Res. A*, **317**, 597–600.
Valek, B. C., Tamura, N., Spolenak, R., MacDowell, A. A., Celestre, R. S., Padmore, H. A., Bravman, J. C., Brown, W. L., Batterman, B. W. & Patel, J. R. (2001). *Mater. Res. Soc. Proc.* **673**, P7.7.1–P.7.7.6.
Venkatraman, R., Bravman, J. C., Nix, W. D., Davies, P. W., Flinn, P. A. & Fraser, D. B. (1990). *J. Electron. Mater.* **19**, 1231–1237.

Received 3 July 2002 • Accepted 20 November 2002